Mon. Not. R. Astron. Soc. **000**, 1–16 (2011) Printed 12 October 2011 (MN LaTeX style file v2.2)

On the Effects of Line-of-Sight Structures on Lensing Flux-ratio Anomalies in a ΛCDM Universe

D. D. Xu[1,2⋆], Shude Mao[1,3], Andrew P. Cooper[4], Liang Gao[1], Carlos S. Frenk[5]
Raul E. Angulo[4], John Helly[5]
[1] *National Astronomical Observatories, Chinese Academy of Sciences, Beijing, 100012, China*
[2] *Argelander-Institut für Astronomie, Universität Bonn, Auf dem Hügel 71, 53121 Bonn, Germany*
[3] *Jodrell Bank Centre for Astrophysics, the University of Manchester, Alan Turing Building, Manchester M13 9PL, United Kingdom*
[4] *Max-Planck Institut Für Astrophysik, Karl-Schwarzshild-Straße 1, 85740 Garching, Germany*
[5] *Institute for Computational Cosmology, Dept. of Physics, University of Durham, South Road, Durham DH1 3LE, United Kingdom*

Accepted ...... Received ...... ; in original form......

ABSTRACT
The flux-ratio anomalies observed in multiply-lensed quasar images are most plausibly explained as the result of perturbing structures superposed on the underlying smooth matter distribution of the primary lens. The cold dark matter cosmological model predicts that a large number of substructures should survive inside larger halos but, surprisingly, this population alone has been shown to be insufficient to explain the observed distribution of the flux ratios of quasar's multiple images. Other halos (and their own subhalos) projected along the line of sight to the primary lens have been considered as additional source of perturbation. In this work, we use ray tracing through the Millennium II simulation to investigate the importance of projection effects due to halos and subhalos of mass $m > 10^8 h^{-1} M_{\odot}$ and extend our analysis to lower masses, $m \geqslant 10^6 h^{-1} M_{\odot}$, using Monte-Carlo halo distributions. We find that violations of the cusp−caustic relation caused by line-of-sight haloes are comparable to (or even larger than) those caused by intrinsic substructures. The magnitude of the violation depends strongly on the density profile and concentration of the intervening halos, but clustering plays only a minor role. For a typical lensing geometry (lens at redshift 0.6 and source at redshift 2), background haloes (behind the main lens) are more likely to cause a violation than foreground halos. The combined effect of substructures within the lens and along the line of sight in a ΛCDM universe results in a cusp-violation probability from lensing flux-ratio observations of ∼20%. This is enough to reconcile the model with current data, but larger samples are required for a stronger test of the theory.

Key words: Gravitational lensing - dark matter - galaxies: ellipticals - galaxies: formation

1 INTRODUCTION

In the cold dark matter (CDM) cosmogony, galaxies are biased tracers of a filamentary "cosmic web" of collapsed regions in the matter density field – dark matter haloes. The excellent agreement between the predictions of this model and observations of the large-scale clustering of galaxies provides compelling support for CDM. However, on the scale of individual dark haloes, the model makes a number of predictions that have yet to be fully verified: cuspy halo density profiles and a large population of surviving dark matter substructures. These substructures are the cores of accreted CDM haloes that persist as long-lived gravitationally bound subhaloes (Gao et al. 2004; Diemand et al. 2008; Springel et al. 2008). Therefore, measurements of halo density profiles and of the subhalo abundance are crucial tests of the cosmological model.

Galaxies and their dark matter haloes can act as strong gravitational lenses, producing distorted and even multiple images of more distant galaxies and quasars. The distribution and properties of these images provide sensitive probes of the mass distribution in the lens. In some multiply-lensed quasar systems, simple parametric mass models can fit image positions well, but not their flux ratios. Such anoma-

⋆ E-mail: xudd@astro.uni-bonn.de

lies are interpreted as evidence for complex substructures in lensing galaxies[1] (Mao & Schneider 1998; Metcalf & Madau 2001; Metcalf & Zhao 2002; Chiba 2002; Metcalf et al. 2004; Sugai et al. 2007; McKean et al. 2007; More et al. 2009; MacLeod et al. 2009).

On scales probed by galactic strong lensing (typically a few kiloparsecs), predictions from CDM simulations have been compared with observed flux-ratio anomalies (e.g. Dalal & Kochanek 2002; Bradač et al. 2004; Metcalf & Amara 2010). Several studies have concluded that the predicted abundance of dark matter substructures in the strong-lensing regions of galaxy-sized haloes is not sufficient to explain the statistics of the currently available sample of known anomalous lenses (Mao et al. 2004; Amara et al. 2006; Macciò & Miranda 2006; Chen et al. 2011).

In any smooth lens potential producing multiple images of a single source, a specific magnification ratio (here equivalent to a flux ratio) of the three most strongly-magnified images will approach zero asymptotically as the source approaches a cusp of the tangential caustic. This is known as the "cusp-caustic relation" (see Eq. 3 below) (Blandford & Narayan 1986; Schneider & Weiss 1992; Zakharov 1995; Keeton et al. 2003). Structures, either within a lensing galaxy or projected by chance along the line of sight, will perturb the potential and alter the flux of one or more images, resulting in a violation of the cusp-caustic relation. These violations are extreme cases of flux-ratio anomalies.

Xu et al. (2009, 2010) analyzed flux-ratio distributions of multiple-imaged background quasars in simulated lensing systems, using six $\sim 10^{12}\mathrm{M}_{\odot}$ CDM haloes and their substructure populations (subhaloes and streams) from the Aquarius project (Springel et al. 2008). The effects of baryonic substructures (satellite galaxies and globular clusters) were also investigated. These exceptionally high resolution simulations confirmed that the substructure abundance (in the critical region of a Milky Way-mass lens) predicted by the CDM model is too low to explain the observed frequency of cusp-caustic violations.

This apparent deficiency of substructures is not yet a strong challenge to CDM, in part because the sample of observed lenses is extremely small. Furthermore, dark matter haloes and subhaloes are present along the entire line of sight from the source to the observer, not just in the lens itself. These independent haloes projected in front of and behind the lens can also induce perturbations to the lensing potential and thus cause flux-ratio anomalies (Chen et al. 2003; Wambsganss et al. 2005; Metcalf 2005a,b; Miranda & Macciò 2007; Puchwein & Hilbert 2009).

In particular, Chen et al. (2003) used the cross-section (optical depth) method to calculate the effect of both subhaloes intrinsic to the main lens and line-of-sight haloes. They found that the former would dominate the total lensing cross-section, although the exact percentage was highly sensitive to the spatial distribution of substructures[2]; the latter – line-of-sight haloes, modelled as singular isothermal spheres – would contribute to $\leqslant 10\%$ of the total perturbation. Metcalf (2005a) performed ray-tracing simulations for the line-of-sight lens population ($10^6 M_{\odot} \leqslant m \leqslant 10^9 M_{\odot}$) in a ΛCDM universe, which he compared to several observed systems with measured cusp-caustic ratios. Assuming that haloes have Navarro, Frenk & White (NFW) profiles (Navarro et al. 1996, 1997), he found that the predicted abundance of line-of-sight haloes was enough to explain the observed flux-ratio anomalies of several representative cases. With a slightly different approach and assuming singular isothermal spheres for the line-of-sight haloes, Miranda & Macciò (2007) found that with contributions from the sight-line perturbers, the observed flux-ratio anomalies can be reproduced with a high confidence level.

In this work, we re-examine the perturbing effect of haloes along the entire line of sight from the source to the observer by using N-body simulations to generate strong-lensing sight lines and quantify the flux-ratio distributions for multiply-imaged sources. In §2, we introduce our method for tracing light deflection through multiple lens planes. In §3, we present a summary of the cusp-caustic violations arising from simple perturbation scenarios (varying the density profiles, angular positions and redshifts of the perturbers). In §4, we describe our method for generating "lensing lighcones" in the Millennium II ΛCDM N-body simulation (Boylan-Kolchin et al. 2009). Results from the analysis of these lensing cones are given in §5. In §6 we present results using a Monte-Carlo approach to account for haloes below the mass resolution limit of Millennium II ($\sim 10^8 h^{-1} M_{\odot}$). Our conclusions are given in §7. The cosmology of our lensing simulations is the same as that used for the Millennium-II simulation, with a matter density $\Omega_{\mathrm{m}} = 0.25$, cosmological constant $\Omega_\Lambda = 0.75$, Hubble constant $h = H_0/(100\,\mathrm{km\,s^{-1}\,Mpc^{-1}}) = 0.73$ and linear fluctuation amplitude $\sigma_8 = 0.9$. These values are consistent with cosmological constraints from the WMAP 1- and 5-year data analyses (Spergel et al. 2003; Komatsu et al. 2009), but differ at about the 2σ level from more recent WMAP 7-year determinations (Komatsu et al. 2011). This small offset is of no consequence for the topics addressed in this paper.

2 SIMULATIONS OF LIGHT DEFLECTION THROUGH MULTIPLE LENS PLANES

In Chapter 9 of Schneider et al. (1992), the authors present the theory of light deflection through multiple lens planes. As shown in Fig. 1, haloes are projected near the line of sight at all redshifts between the observer and a source at redshift z_s. The angular position of the source is denoted by $\vec{\beta}^{\star}$, and its final image position is denoted by $\vec{\theta}^{\star}$. The haloes are assumed to be distributed in N lens planes, each at redshift z_i (i=1,2...N, and $z_s = z_{N+1}$). As the light ray passes through each plane, the image position $\vec{\theta}_{i+1}$ (where the light ray intercepts the plane) in the $(i+1)$-th lens plane, which is also the source position $\vec{\beta}_i$ for the i-th plane, is

[1] Apart from quasar images' flux-ratio anomalies, another promising method is to use surface brightness anomalies of lensed galaxies to identify substructures and constrain their properties, see e.g., Vegetti & Koopmans (2009); Vegetti et al. (2009).

[2] A similar conclusion was reached by Xu et al. (2009, 2010); see also Nierenberg et al. (2011) for the observed spatial distribution of luminous satellites in early-type galaxies.

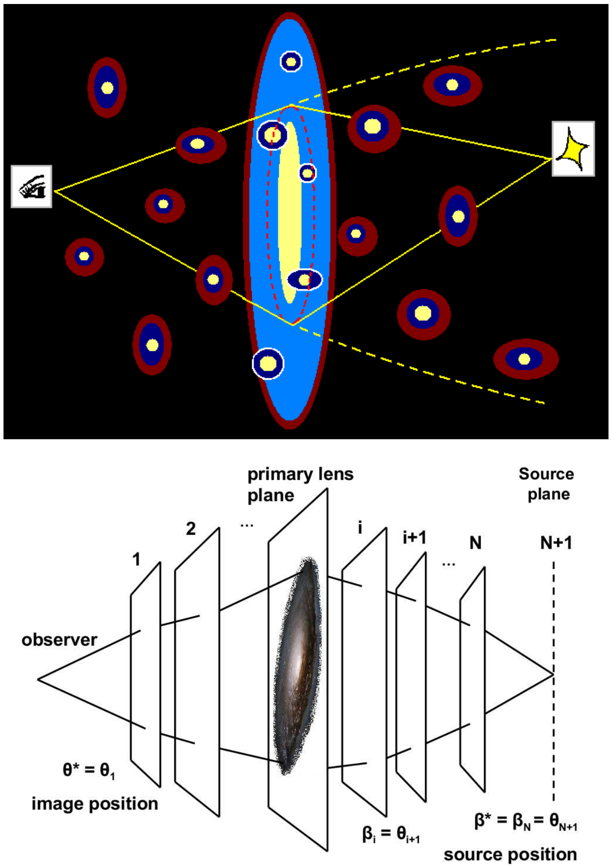

Figure 1. An illustration (top) of a light ray propagating through intergalactic space from a lensed quasar to an observer. The primary galaxy/halo at intermediate redshift causes image splitting due to its strong lensing effect. Both intrinsic substructures (satellite subhaloes and galaxies) in the primary lens and intergalactic haloes along the line of sight perturb the lensing potential and give rise to anomalous flux ratios between the images. The corresponding illustration of ray tracing through multiple lens planes is given in the bottom panel.

related to $\vec{\beta}^{\star}$ and $\vec{\theta}^{\star}$ by the lens equation:

$$\vec{\theta}_{i+1} = \vec{\beta}_i = \vec{\theta}_1 - \sum_{j=1}^{i} \frac{D_{j,i+1}}{D_{i+1}} \vec{\alpha}_j(\vec{\theta}_j), \qquad (1)$$

where $\vec{\theta}_{N+1} = \vec{\beta}_N = \vec{\beta}^{\star}$, and $\vec{\theta}_1 = \vec{\theta}^{\star}$. $\vec{\alpha}_j(\vec{\theta}_j)$ is the deflection angle a light ray undergoes in the j-th plane at $\vec{\theta}_j$. D_{i+1} and $D_{j,i+1}$ are angular diameter distances between the $(i+1)$-th plane and the observer, and between the $(i+1)$-th plane and the j-th plane, respectively. $D_{N+1} = D_s$ is the angular diameter distance of the source. The Jacobian matrix A_i of the mapping between $\vec{\theta}_1$ and the source position $\vec{\beta}_i$ for the i-th plane is given by:

$$A_i = \frac{\partial \vec{\beta}_i}{\partial \vec{\theta}_1} = \frac{\partial \vec{\theta}_{i+1}}{\partial \vec{\theta}_1} = I - \sum_{j=1}^{i} \frac{D_{j,i+1}}{D_{i+1}} \frac{\partial \vec{\alpha}_j}{\partial \vec{\theta}_j} \frac{\partial \vec{\theta}_j}{\partial \vec{\theta}_1} \qquad (2)$$

and $A_N \equiv A_s = \frac{\partial \vec{\beta}_N}{\partial \vec{\theta}_1}$ is the overall Jacobian matrix, describing the mapping relation between $\vec{\beta}^{\star}$ and $\vec{\theta}^{\star}$. The magnification μ is then given by $\mu = \det A_s^{-1}$.

Images of any given background source can be accurately and efficiently identified using the Newton-Raphson method, once the mapping relation (the overall Jacobian matrix $A_s = \frac{\partial \vec{\beta}_N}{\partial \vec{\theta}_1}$) is obtained. We determine the Jacobian matrix numerically, as follows. For each lens plane, a rigid grid of 1000×1000 is applied to cover a central region of $5'' \times 5''$. Source positions $\vec{\beta}_N(\vec{\theta}_1)$ that correspond to grid points $\vec{\theta}_1$ in the first lens plane (which is also the final image plane) are calculated through the multi-plane lens equation (Eq. 1). An arbitrary light ray propagating through a lens plane will not necessarily hit a grid point of the mesh that covers that plane. Therefore, for any given position $\vec{\theta}_i$ of the i-th lens plane, the deflection angle $\vec{\alpha}_i(\vec{\theta}_i)$ is obtained by linear interpolation using the values for the four nearest grid points. Once $\vec{\beta}_N(\vec{\theta}_1)$ is obtained, the Jacobian matrix $A_s = \frac{\partial \vec{\beta}_N}{\partial \vec{\theta}_1}$ can be derived using finite differencing with the five-point stencil method. We use our multi-plane ray tracing code with a resolution of $0.005''$/pix in the lens and image planes, which we find sufficient to accurately reproduce the lensing properties of a number of simple analytical cases.

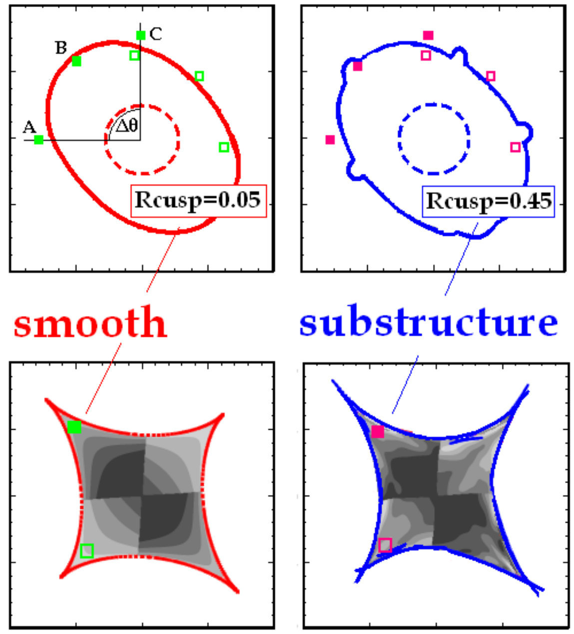

Figure 2. An illustration of how the presence of substructures affects the cusp-caustic relation. The upper panels show the critical curves in the image plane; the bottom panels are the contour maps of $R_{\rm cusp}$ for sources within the tangential caustic in the source plane. Squares indicate positions of close triple images and the corresponding sources in the two planes. The image opening angle $\Delta\theta$ is labelled for one case in the top left panel. The left column shows cases with a smooth lens potential. In the right column, we show cases where substructures are present. The cusp-caustic relation is violated when a perturbing structure is projected near the image positions around the critical curve (see text).

3 ANOMALOUS FLUX RATIOS AND CUSP-CAUSTIC VIOLATIONS

The cusp-caustic relation (Blandford & Narayan 1986; Schneider & Weiss 1992; Zakharov 1995; Keeton et al. 2003)

Table 1. Four-image quasar lensing systems with $\Delta\theta \leqslant 120^\circ$ measured at radio wavelengths (CLASS).

Systems	$\Delta\theta$ ($\circ$)	$R_{\rm cusp}$	Reference
(1) B2045+265	34.9	0.501	Fassnacht et al. (1999) Koopmans et al. (2003)
(2) B0712+472	76.9	0.255	Jackson et al. (1998) Koopmans et al. (2003)
(3) B1422+231	77.0	0.187	Patnaik et al. (1999) Koopmans et al. (2003)
(4) MG0414+053	101.5	0.227	Katz et al. (1997)
(5) B1555+375	102.6	0.417	Marlow et al. (1999) Koopmans et al. (2003)

is defined as:

$$R_{\rm cusp} \equiv \frac{|\mu_A + \mu_B + \mu_C|}{|\mu_A| + |\mu_B| + |\mu_C|} \rightarrow 0 \quad (3)$$

when $\mu_{\rm total} = |\mu_{\rm A}| + |\mu_{\rm B}| + |\mu_{\rm C}| \rightarrow \infty$. μ denote the magnifications of the three closest images (A, B and C) of a background point source located near a cusp of the tangential caustic (as shown in Fig. 2). Observationally, source positions cannot be directly measured – instead, an image opening angle is often used as an indicator of the proximity of a source to the nearest cusp of the tangential caustic. This opening angle $\Delta\theta$ is measured between lines joining the centre of the lens to the two outer images A and C. As the source moves outwards (towards the nearest cusp), $\Delta\theta \rightarrow 0$, $\mu_{\rm total} \rightarrow \infty$, and $R_{\rm cusp}$ will go to zero asymptotically. This relationship holds for any smooth lens potential.

Fig. 2 illustrates how perturbing structures change the cusp-caustic relation. The upper panels show the critical curves in the image plane, and the bottom panels are contour maps of $R_{\rm cusp}$ for sources within the tangential caustic in the source plane. Left and right columns show smooth lens potentials and lens potentials with substructures, respectively. Substructures located near the critical curve will affect images nearby and result in significantly larger values of $R_{\rm cusp}$, violating the predicted ratios of image magnifications (fluxes) given by Eq. (3).

3.1 Observational samples

Multiple images of lensed quasars with small $\Delta\theta$ are ideal cases to examine violations of the cusp-caustic relation and can be used to put constraints on the properties of perturbing structures. This is especially true when their fluxes are measured in the radio and mid-infrared, as the interpretation of optical and near-infrared flux ratios is complicated by stellar microlensing and dust extinction. At the present time, only five cusp-geometry lensing systems with image opening angle $\Delta\theta \leqslant 90^\circ$ are known. These were used for statistical comparisons to the simulations in our previous work (Xu et al. 2009, 2010). All five cases have surprisingly large $R_{\rm cusp}$ values which are difficult to explain with simple smooth lens models. Of these five (flux-ratio measurements), two that were obtained in the optical have been proven to be affected by microlensing; the other three were from the CLASS survey (Browne et al. 2003; Myers et al. 2003) at radio wavelengths and are thought to be more secure cases of perturbations due to substructures in the lens.

Table 2 of Chen et al. (2011) lists all of the currently observed $R_{\rm cusp}$-$\Delta\theta$ pairs for systems with four distinct point-like images of quasars lensed by one single galaxy. Our Table 1 lists those with their flux ratios measured in the radio and their image opening angles $\Delta\theta \leqslant 120^\circ$. In this work, we have calculated the $R_{\rm cusp}$ distribution for all possible source positions that have close-triple image opening angle $\Delta\theta \leqslant 120^\circ$ under different perturbing scenarios.

3.2 Statistical measures for the cusp-caustic violation: $P(\geqslant R_{\rm cusp}|\Delta\theta \pm 2.5^\circ)$ and $P^{90}(R^{0.187}_{\rm cusp})$

Given a simulated lensing system, we compare to the observations in Table 1 by generating a large number of realisations of background sources with $\Delta\theta \leqslant 120^\circ$. We calculate $R_{\rm cusp}$ for each realisation and evaluate $P(\geqslant R_{\rm cusp}|\Delta\theta \pm 2.5^\circ)$ for this ensemble of realisations. This is defined as the probability for $R_{\rm cusp}$, measured for sources with image opening angles $\in [\Delta\theta - 2.5^\circ,\ \Delta\theta + 2.5^\circ]$ (i.e. within a five-degree opening-angle span centred at $\Delta\theta$) to be larger than a particular threshold value. Lenses with more perturbations will result in large $R_{\rm cusp}$ values for many source positions and thus have a higher $P(\geqslant R_{\rm cusp}|\Delta\theta \pm 2.5^\circ)$ than lenses with fewer perturbations.

We illustrate our use of the $P(\geqslant R_{\rm cusp}|\Delta\theta \pm 2.5^\circ)$ in Fig. 3. The top panel shows a typical example of a close triple image configuration for cusp sources with $\Delta\theta \leqslant 120^\circ$. In this case, the lensing galaxy has a (smooth) singular isothermal ellipsoidal (SIE) profile (see Keeton & Kochanek (1998) for notations of b_I, $b_{\rm SIE}$, q_3, and s_0 herebelow) with lensing strength $b_I = 0.6''$ and axis ratio $q_3 = 0.8$, and is located at redshift $z_d = 0.6$; the source redshift is $z_s = 2$. The corresponding contour map of $P(\geqslant R_{\rm cusp}|\Delta\theta \pm 2.5^\circ)$ in the $R_{\rm cusp}$-$\Delta\theta$ plane is given in the middle panel. Also plotted are the radio measurements for the currently best available sample (listed in Table 1). These are clearly inconsistent with the smooth-lens $R_{\rm cusp}$ distribution.

When we include the substructures within the lensing galaxy and its dark matter halo, the regular $R_{\rm cusp}$ distribution for a smooth lens potential disappears. The bottom panel in Fig. 3 shows the average distribution of $P(\geqslant R_{\rm cusp}|\Delta\theta \pm 2.5^\circ)$ when including the subhalo population from the Aquarius simulations (Xu et al. 2009). At small $\Delta\theta$, violations are more significant than on larger scales. The smallest $R_{\rm cusp}$ measured among all observed cusp-caustic systems is 0.187 (from B1422). In Xu et al. (2009), we calculated the mean violation probability $P^{90}(R^{0.187}_{\rm cusp})$ for $R_{\rm cusp}$ to be larger than or equal to 0.187, computed over all realizations with $\Delta\theta \leqslant 90^\circ$. $P^{90}(R^{0.187}_{\rm cusp})$ was found to be $\sim$10%. We concluded that it is difficult to explain the observed $R_{\rm cusp}$ distribution (especially at larger $\Delta\theta$) with a subhalo population similar to that produced in the Aquarius simulations. This motivates the search for other sources of perturbations to the lens potential.

3.3 Simple perturbation scenarios with different halo redshifts, masses, profiles and concentrations

A number of parameters determine the importance of these perturbers for creating violations to the cusp-caustic rela-

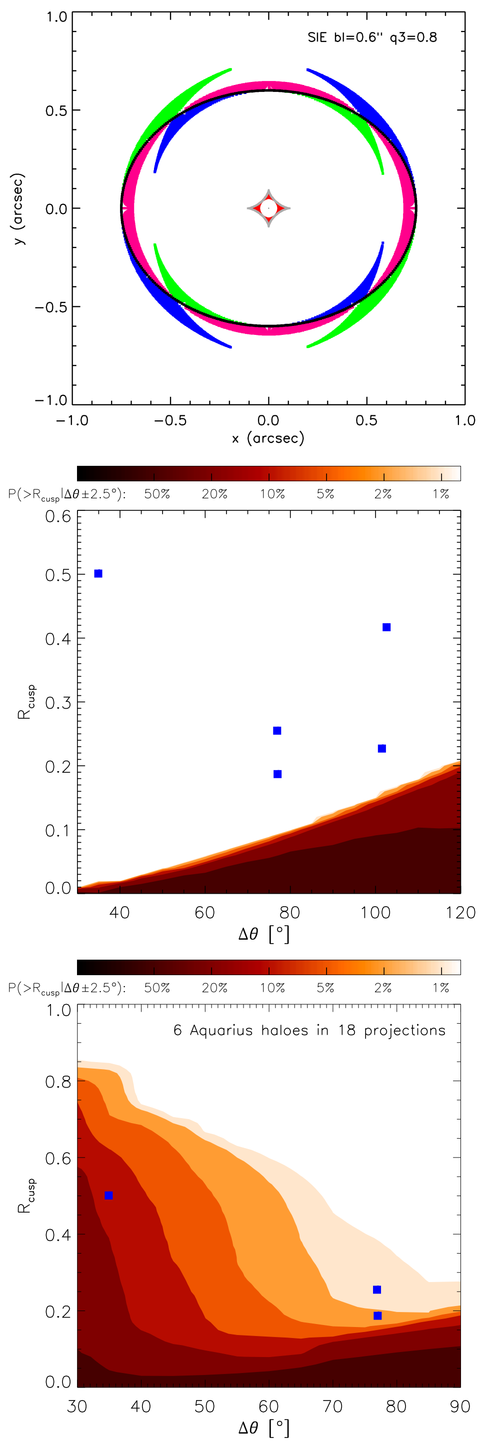

Figure 3. Top panel: Close triple image configurations for a SIE lens with $b_I = 0.6''$ and $q_3 = 0.8$. The critical curve of the lens is shown in black and its caustics in grey. The regions sampled by "cusp sources" are shown in red, and the corresponding distributions of the three images are shown as green, pink and blue regions around the critical curve. Middle panel: the corresponding probability contour map for $P(\geqslant R_{\rm cusp}|\Delta\theta \pm 2.5°)$. Contour levels of 1%, 2%, 5%, 10%, 20% and 50% (from top to bottom) are plotted. Blue squares are the five radio measurements (with $\Delta\theta \leqslant 120°$) so far available. Bottom panel: the average probability contour map (for $\Delta\theta \leqslant 90°$) of violations due to substructures in the Aquarius haloes (using results from Xu et al. 2009).

tion: most significant are their masses, density profiles, redshifts and impact parameters to the line of sight. Before presenting the results from general lines of sight taken from N-body simulations, we first show several simple perturbation scenarios to illustrate, individually, the effects of these different parameters, in the case of a single perturbing halo.

Fig. 4 shows critical curves and caustics produced by a main-lens potential of an isothermal ellipsoid with $b_I = 0.6''$, $q_3 = 0.8$ and core size $s_0 = 0.05''$, located at $z_d = 0.6$ for a source at redshift $z_s = 2$, plus a perturber of $m = 10^{10} M_\odot$ modelled with a truncated singular isothermal sphere. The panels in this figure correspond to different scenarios. In the upper row the perturber's angular position is fixed (outside the tangential critical curve), and we vary its redshift: $z = 0.4$ (foreground), $z = 0.6$ (in the main-lens plane) and $z = 1.4$ (background). In the lower row, we fix the redshift of the perturber to the main lens plane ($z = 0.6$) and change its impact parameter, such that it is projected within, on top of and outside the tangential critical curve (left to right panels, respectively). Wiggles and swallow tails are introduced to the critical lines and caustics by the added perturbing structure; massive perturbers (or those with compact density profiles) can even cause a secondary set of criticals and caustics. Images located around these wiggle features violate the cusp-caustic relation most strongly.

Fig. 5 shows the contour maps of $P(\geqslant R_{\rm cusp}|\Delta\theta \pm 2.5°)$ in the $R_{\rm cusp}$-$\Delta\theta$ plane for the different scenarios above. Violation patterns as a function of image opening angle $\Delta\theta$ vary with the positions and redshifts of the perturbers. Notice that at redshifts greater than that of the primary lens, the cone of light rays starts decreasing in size towards the source. This means a "background" perturber that appears to be projected close to the critical curve (where images normally form) could actually be far away from the light ray. Such perturbers would be less effective in causing convergence fluctuations than their foreground counterparts (they would still contribute to the shear field). However, depending on the distribution of the primary lens and the source, there could be many more background structures affecting the light ray than those in the foreground (see §5).

The mass and density profile of a perturber also affect the production of flux-ratio anomalies (and cusp-caustic violations) by altering the effective cross-section. Singular isothermal spheres have been found to be a good approximation for the inner density profiles of relatively massive haloes (Rusin et al. 2003; Treu & Koopmans 2004; Rusin & Kochanek 2005; Koopmans et al. 2006, 2009), where baryons are thought to dominate their central potentials. This effect may be less important in smaller haloes, where the density profile is more likely to be well approximated by the NFW distribution characteristic of CDM haloes in N-body simulations (Navarro et al. 1997). Nevertheless, there is still much controversy whether observed low-mass haloes around dwarf galaxies have core-like shallow profiles (Oh et al. 2011).

In the simple scenarios presented below and in our line-of-sight lensing simulations (see §5 and §6), we model perturbing haloes either as truncated singular isothermal

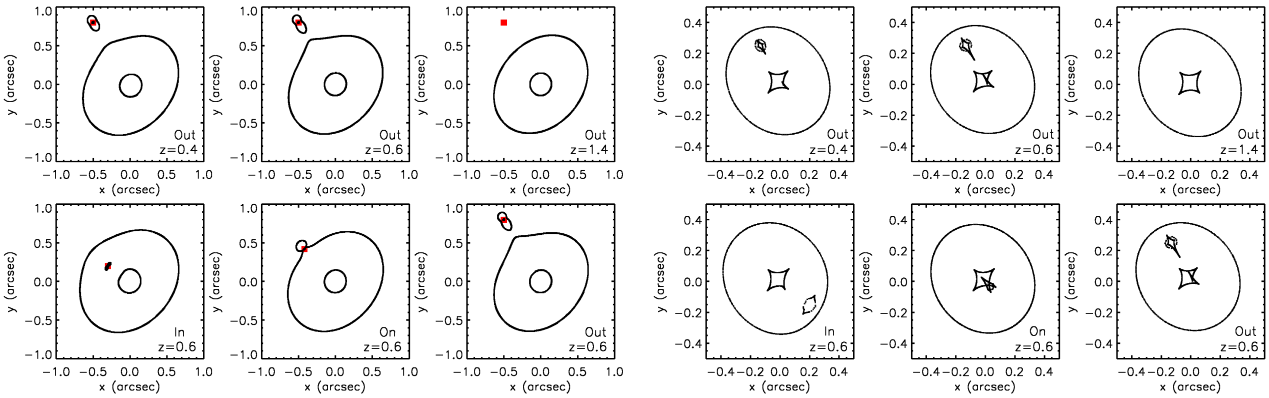

Figure 4. Critical curves (six panels on the left) and caustics (six panels on the right) produced by the same smooth lens potential plus a $m = 10^{10} M_{\odot}$ perturber (indicated by red squares), modelled by a truncated singular isothermal sphere. Top row: the perturber's angular position is fixed and its redshift set at $z = 0.4$ (in the foreground, left panel), $z = 0.6$ (in the primary lens plane, middle panel) and $z = 1.4$ (in the background, right panel). Bottom row: The redshift of the perturber is fixed ($z = 0.6$) and its impact parameter is changed from inside the tangential critical curve (left panel, labelled as "In"), to overlapping (middle panel, labelled as "On") to outside (right panel, labelled as "Out"). Parameters are noted in each panel. Note the wiggles induced in the critical curves and the production of secondary critical curves and caustics.

.

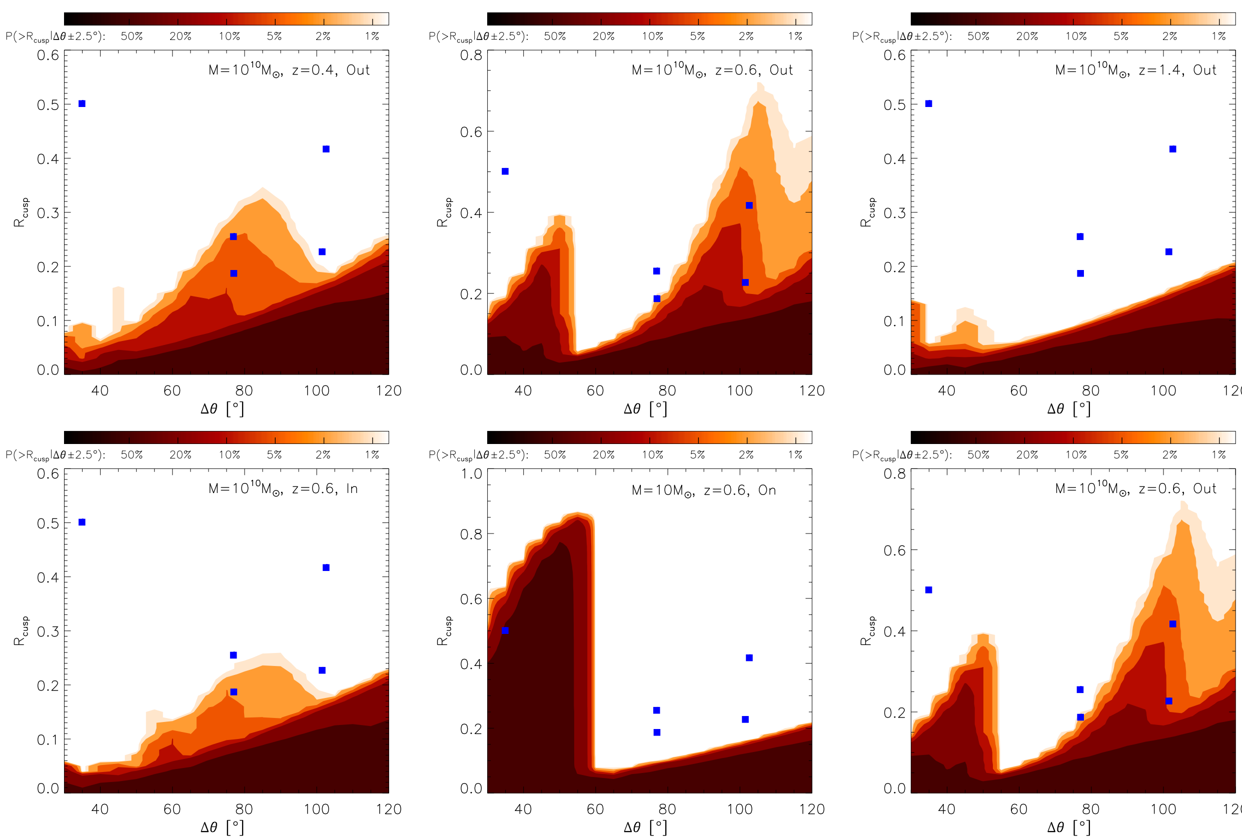

Figure 5. Corresponding probability contour maps of $P(\geqslant R_{\rm cusp}|\Delta\theta \pm 2.5^{\circ})$ for cases presented in Fig. 4. Symbols and contour levels are the same as in Fig. 3. The top row presents cases where a perturber (of $10^{10} M_{\odot}$) is projected at the same angular position as shown in the upper panels of Fig. 4, but located at different redshifts: $z = 0.4$ (foreground), $z = 0.6$ (in the main-lens plane) and $z = 1.4$ (background); the second row shows cases where the perturber is located at $z = 0.6$ but projected at three different angular positions as shown in the lower panels of Fig. 4.

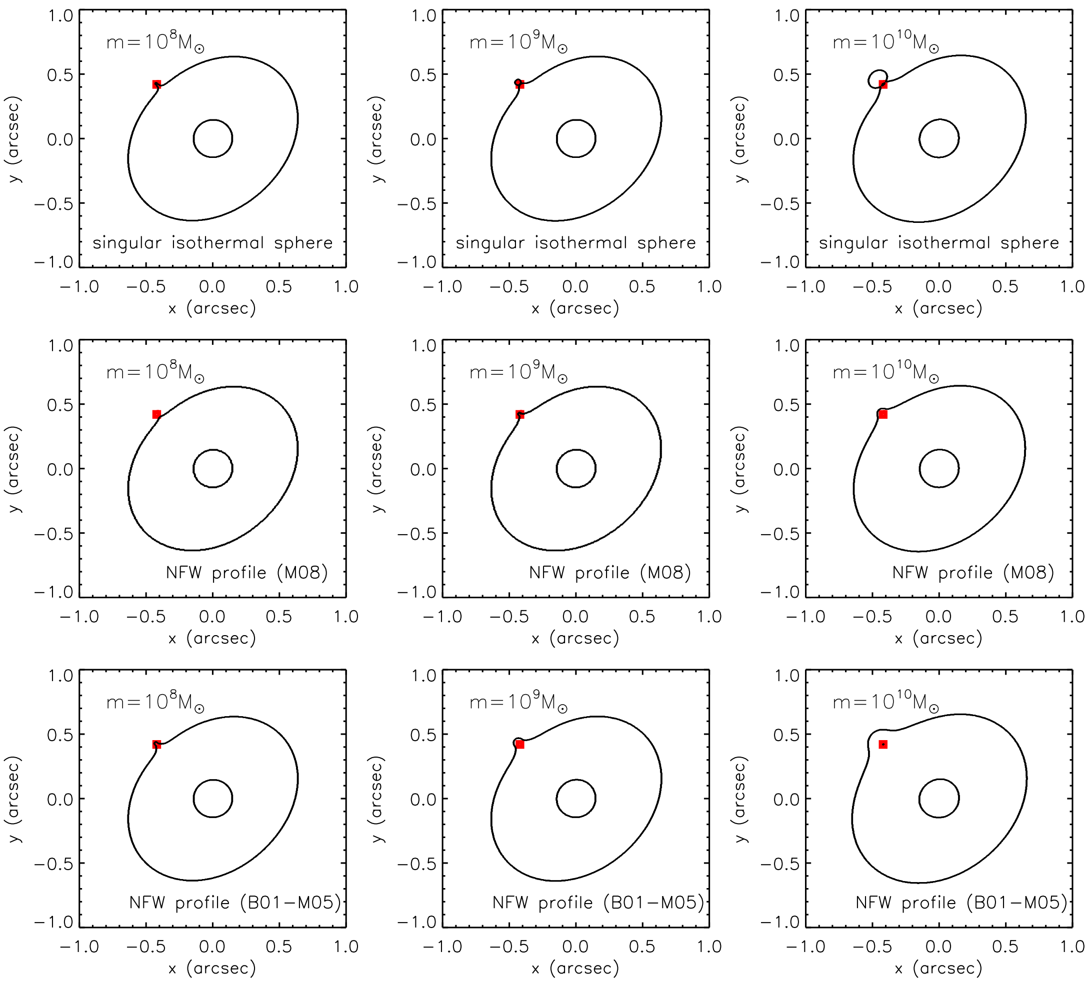

Figure 6. Critical curves for smooth lens potential with a single perturbing halo (located at $z = 0.6$), plotted as a red square. In columns from left to right the perturber has a mass of $10^8 M_\odot$, $10^9 M_\odot$, and $10^{10} M_\odot$, respectively. The rows from top to bottom correspond to different assumptions for the density profile: a truncated singular isothermal sphere, a truncated NFW profile with the M08 concentration-mass relation, and a truncated NFW profile with the B01-M05 concentration-mass relation, respectively.

spheres[3] or truncated NFW profiles, normalized with their masses and truncated at their virial radii. We follow the convention of defining the virial radius as r_{200}, the radius within which the mean halo density is 200 times the critical density of the Universe (at the appropriate redshift z). The mass enclosed within r_{200} is denoted as M_{200}. For the NFW profile, the concentration parameter is $C_{200} \equiv r_{200}/r_\mathrm{s}$, where r_s is the scale radius. This parameter is thought to correlate with mass M_{200} and redshift z. A number of concentration-mass relations have been proposed in the literature, based on N-body simulations.

In this work, we adopt the concentration-mass relation of Macciò et al. (2008) (hereafter M08) wherever we model perturbers as truncated NFW profiles. The fitting formula (for a WMAP-1 cosmology, close to that of the Millennium-II simulation) is given by:

$$C_{200}(M_{200}, z) = \frac{10^{0.917}}{[H(z)/H_0]^{2/3}} \left(\frac{M_{200}}{10^{12} M_\odot} \right)^{-0.104}, \qquad (4)$$

where $H^2(z) = H_0^2[\Omega_\Lambda + \Omega_m(1+z)^3]$.

The concentration-mass relation of Bullock et al. (2001) was used by Metcalf (2005a,b) to study how line-of-sight haloes ($10^6 M_\odot \leqslant m \leqslant 10^9 M_\odot$) contribute to the flux anomaly problem. The adopted fitting formula was given by (Metcalf 2005b):

$$C_{200}(M_{200}, z) = \frac{14}{1+z} \left(\frac{M_{200}}{10^{12} M_\odot} \right)^{-0.15}. \qquad (5)$$

To compare with Metcalf (2005a,b), we also perform our analysis using this alternative concentration-mass relation, hereafter referred to as B01-M05.

Fig. 6 shows how these different assumptions for the mass, density profile and concentration-mass relation of a perturber change the total critical curves produced by

[3] A singular isothermal sphere may not be a realistic model for small haloes. We adopt this model for ease of comparison with previous work, e.g. Chen et al. (2003).

a primary lens at $z = 0.6$ and the perturbing halo located at the same redshift and with a mass of $M_{200} = [10^8 M_\odot,\ 10^9 M_\odot,\ 10^{10} M_\odot]$. A different density profile (a truncated singular isothermal sphere, a truncated NFW profile with the M08 concentration-mass relation and a truncated NFW profile with the B01-M05 concentration-mass relation) is assumed in each row of Fig. 6. Different distortions to the critical curve correspond to different levels of violations in the smooth-lens flux-ratio relationship.

The mass dependence of the violation pattern has been studied systematically, with results presented in §6, which also includes a discussion of effects from different concentration-mass relations and from allowing scatter in the concentration on the overall cusp-violation probabilities.

In this section we have illustrated the effects of varying the redshift, impact parameter, mass and density profile of a single perturbing halo. In practice, perturbations could arise anywhere along the line of sight and from many different haloes. The overall perturbation is far more complicated than any of the simple cases presented here. In the following sections, we use cosmological N-body simulations to obtain self-consistent and realistic distributions of perturbers along strong lensing sight lines, and estimate the net perturbation and the likelihood of the observed flux ratio violations.

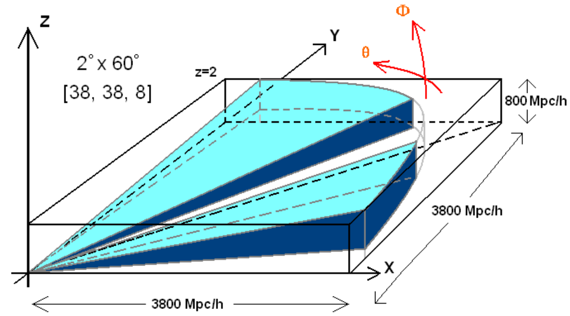

Figure 7. The geometry of the replicated box for light-cone generation: the MS-II simulation box of $100h^{-1}$ Mpc is repeated in its X, Y and Z dimensions as many times as needed to cover the desired redshift range and angular size. For a source redshift of $z_s = 2$, the total dimension of the combined box is set to be $38 \times 38 \times 8$, in units of one Millennium-II simulation box. An observer is put at the origin (0, 0, 0) of this box. The position angle pair (θ, ϕ) of a given line-of-sight vector are defined as the angles measured from the ZX- and XY-plane, respectively. The simulated sky we have looked at is then two $2^\circ \times 30^\circ$ stripes, which cover $10^\circ \leqslant \theta \leqslant 40^\circ$ and $50^\circ \leqslant \theta \leqslant 80^\circ$, and $10^\circ \leqslant \phi \leqslant 12^\circ$. Directions along the axes (with $\leqslant 10^\circ$) and along $\theta \sim 45^\circ$ have been excluded to avoid significant structure repetition.

4 LENSING LINES OF SIGHT FROM COSMOLOGICAL SIMULATIONS

4.1 Constructing lensing cones from MS-II

The Millennium-II simulation (MS-II; Boylan-Kolchin et al. 2009) is an N-body simulation of a cubic cosmological volume with a comoving side length of $100h^{-1}$ Mpc, at a spatial resolution of $1h^{-1}$ kpc and mass resolution of $6.89 \times 10^6 h^{-1} M_\odot$. The cosmological parameters of MS-II are the same as those of the earlier Millennium and Aquarius simulations, consistent with the WMAP-1 results. MS-II provides us with the large-scale distributions of a cosmological sample of dark matter haloes. When tracing lensing sight lines through this simulation, we use the following method to determine where haloes cross the past light cone of a fiducial observer (for more details, see Angulo 2008).

We start by replicating the $100h^{-1}$ Mpc simulation box in its X, Y and Z dimensions, as many times as we need to cover the desired redshift range (along the sight line) and angular size (transverse to the sight line). For computational efficiency we only let the combined box go to the source redshift in the X and Y dimensions, and keep the number of replications in the Z dimension to a minimum. As illustrated in Fig. 7, the observer is located at the origin (0, 0, 0) in one corner of this replicated box. Assuming a source redshift of $z_s = 2$, the total dimension of the combined box is chosen to be $38 \times 38 \times 8$, in units of one Millennium-II simulation box. The position angles (θ, ϕ) of a given line-of-sight vector are defined as the angles measured from the ZX- and XY-plane, respectively. The simulated sky into which we trace sight lines is then two $2^\circ \times 30^\circ$ stripes, which cover $10^\circ \leqslant \theta \leqslant 40^\circ$ and $50^\circ \leqslant \theta \leqslant 80^\circ$, and $10^\circ \leqslant \phi \leqslant 12^\circ$. Directions along the X and Y axes (with $\leqslant 10^\circ$) and along $40^\circ \leqslant \theta \leqslant 50^\circ$ have been excluded to avoid significant repetition of structures in the replicated box.

Haloes at each simulation snapshot (corresponding to a particular redshift) are identified using the Friends-of-Friends algorithm (Davis et al. 1985). Haloes also contain many subhaloes; these are identified using the SUBFIND algorithm (Springel 2005). The minimum mass of subhaloes resolved by the simulation is $1.4 \times 10^8 h^{-1} M_\odot$ (corresponding to 20 particles). Haloes at different snapshots are linked together by an algorithm for defining their merging history (Helly et al. 2003). We follow haloes in each of these merger trees and predict their trajectories (in the replicated box) between every two adjacent snapshots. In this way, we can find the exact redshift and comoving position of a halo at the moment it crosses the past light cone of the observer. When a halo crosses the light cone, all its subhaloes are assumed to cross at the same redshift. We assume that the relative positions of these subhaloes at the light-cone crossing time are the same as in the previous snapshot.

Hereafter, we will use the term "lensing cone" to refer to the observer's light cone that encloses a particular lensing sight line towards a certain direction in the sky (and out to the source redshift). All haloes that cross the past light cone are checked to see if they are physically within a given lensing cone. If so, their positions, redshifts, masses and half mass radii are stored for lens modelling. All lensing cones are $50'' \times 50''$-wide, out to a source redshift $z_s = 2$, and contain a primary lens around redshift $z_d = 0.6$ (typical source and lens redshifts for the observed quasar lensing systems).

To build up our lensing cone catalogue, we randomly select about 300 directions in the $2^\circ \times 60^\circ$ simulated sky, each of which goes through at least one galaxy-scale

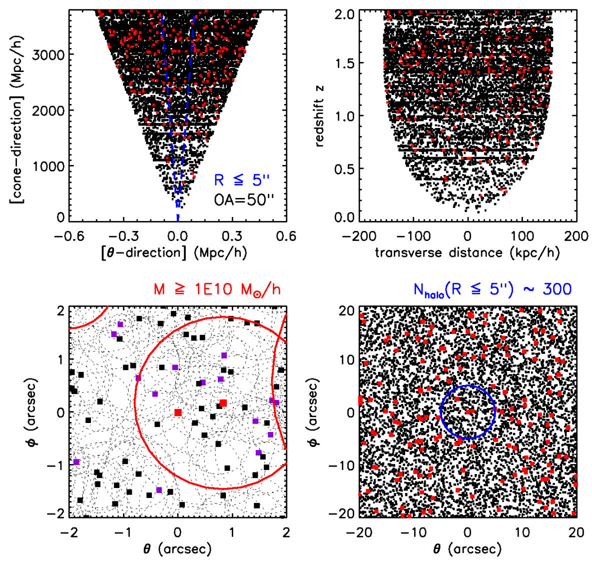

Figure 8. The halo distribution within an example lensing cone in a slice of depth $3800h^{-1}$ Mpc (in co-moving distance), out to a redshift of $z = 2$. The cone covers a region of $50'' \times 50''$. In all four panels, haloes and subhaloes are plotted as black squares; those more massive than $10^{10}M_\odot$ are shown by red squares. The central region of radius $R \leqslant 5''$ is indicated with blue lines in both top left and bottom right panels. Top left: the projected cone geometry in comoving distance. Top right: same lensing cone, shown in the $redshift - physical\ distance$ plane. Bottom left: the central $4'' \times 4''$ region of the light cone projected in the sky, where the main tangential critical curves form; subhaloes are indicated by purple squares in this panel, circles in solid red and dashed black indicate the half-mass radii of haloes (and subhaloes). Bottom right: an expanded view, showing haloes and subhaloes projected within the central $40'' \times 40''$ of the light cone.

halo with a mass above $10^{12}h^{-1}M_\odot$ located at redshift $|z - 0.6| \leqslant 0.02$ in the replicated box. This ensures that the primary haloes we select are responsible for producing multiple images of the $z_s = 2$ background sources. We have confirmed that these $\sim$ 300 randomly selected primary lenses are representative of mass and circular velocity distributions of ∼23,000 haloes that meet the same selection criteria in the simulated sky.

Fig. 8 shows the geometry and halo distribution of an example lensing cone. On average each lensing cone (of $50'' \times 50''$) contains about $10,000$ $(12,000)$ haloes (subhaloes). Within a projected central region of $R \leqslant 5''$ for strong lensing, there are on average $\sim$ 300 haloes with $m > 10^8h^{-1}M_\odot$ directly contributing to the convergence field. The rest are distributed further out (in projection) and contribute to the shear field of this region in the same way as point masses.

4.2 Ray-tracing through MS-II lensing cones and line-of-sight lens modelling

To carry out calculations for multi-plane light deflection, we assume 60 lens planes distributed with equal spacing in redshift between the observer and the source at $z_s = 2$. In each of these lens planes, a region of $5'' \times 5''$ around the line centre is covered by a 1000×1000 rigid grid in order to calculate the Jacobian matrix A_s (Eq. 2) between the source plane and the final image plane.

Haloes within a lensing cone are projected into these lens planes according to their redshifts. The main lens halo is modelled as an isothermal ellipsoid, for which a universal axis ratio ($q_3 = 0.8$) and core radius ($s_0 = 0.05''$) are assumed. The orientation of the ellipsoid is randomly chosen in the interval of $[0, 2\pi]$. The lensing strength $b_{\rm SIE}$ (related with b_I through $b_I = b_{\rm SIE}e/sin^{-1}e$, where $e = (1-q_3^2)^{1/2}$, see Keeton & Kochanek 1998) is derived through an empirical relationship between halo's virial velocity V_{200} and the velocity dispersion $\sigma_{\rm SIE}$ of the equivalent isothermal ellipsoid (Chae et al. 2006):

$$\frac{\sigma_{\rm SIE}}{200\ {\rm km/s}} \approx \left[\frac{1.17\ V_{200}}{200\ {\rm km/s}}\right]^{0.22} (171\ {\rm km/s} \leqslant V_{200} \leqslant 563\ {\rm km/s}) \quad (6)$$

and $b_{\rm SIE} = 4\pi(\sigma_{\rm SIE}/c)^2 D_{\rm ds}/D_{\rm s}$, where c is the speed of light and $D_{\rm ds}$ and $D_{\rm s}$ are the angular diameter distances between the main lens and the source, and the source and the observer, respectively. The virial velocity V_{200} is obtained from halo mass M_{200} and its virial radius r_{200} through $V_{200}^2 = GM_{200}/r_{200}$. Our requirement that the main lens be more massive than $10^{12}h^{-1}M_\odot$ implies a weighted mean lensing strength $b_{\rm SIE} = 0.84''$, derived from an average $\sigma_{\rm SIE}$ of $222\,{\rm km\,s^{-1}}$ for our sample of $\sim$ 300 primary lenses.

Within each lensing cone, haloes with projected profiles that are completely outside the central $5'' \times 5''$ region are treated as point masses. Those within this region are assigned a density profile: as described above, we investigate three distinct choices of this profile (singular isothermal sphere, NFW with the M08 concentration-mass relation, and NFW with the B01-M05 concentration-mass relation). All halo profiles are normalized to their masses M_{200} and truncated at the virial radii r_{200}; subhaloes are truncated at two times their half mass radii.

For each line of sight, deflection angles are individually calculated for the equivalent isothermal ellipsoid of the main lens and for all line-of-sight (sub)haloes, and are tabulated to the meshes at different lens planes. Through ray tracing, source positions $\vec{\beta}_N$ that correspond to the final image plane $\vec{\theta}_1$ are identified, and the final Jacobian matrix $A_s = \frac{\partial\vec{\beta}_N}{\partial\vec{\theta}_1}$ is then derived using the finite differencing method. Images of a given source position are effectively found using the Newton-Raphson iteration method.

5 RESULTS FROM THE MILLENNIUM II SIMULATION

In order to calculate $P(\geqslant R_{\rm cusp}|\Delta\theta \pm 2.5^\circ)$ – the probability distribution in the $R_{\rm cusp} - \Delta\theta$ plane for individual lensing cones, we generate $10,000 \sim 20,000$ cusp sources whose close triple images have image opening angles $\Delta\theta \leqslant 120^\circ$. We have also calculated $P^{90}(R_{\rm cusp}^{0.187})$ for cases with $\Delta\theta \leqslant 90^\circ$ as an overall estimate for cusp-caustic violations to compare with our previous work, in which only cases with $\Delta\theta \leqslant 90^\circ$ were examined for violations (caused by intrinsic substructures within the main lens).

To derive average violation probabilities over all sight lines, we weight $P(\geqslant R_{\rm cusp}|\Delta\theta \pm 2.5^\circ)$ and $P^{90}(R_{\rm cusp}^{0.187})$ of each lensing cone by the quadruple-image lensing cross-section in the source plane (simply the fractional area within the tangential caustic). We do not account for magnification bias among the cusp sources.

Fig. 9 (upper panels) and Table 2 show that if perturbing structures are haloes (and subhaloes) distributed outside the main lens along the line of sight as in the Millennium-II simulation, where such haloes are resolved to $10^8 h^{-1} M_\odot$, they cause a non-negligible amount of cusp violations, comparable to those due to the substructures in the lens itself. However, the violation pattern (as a function of $\Delta\theta$) depends strongly on the density profiles applied to haloes projected near the centre of the line of sight.

5.1 Effects from massive line-of-sight haloes

We have also investigated the effect from line-of-sight haloes more massive than $10^{10} h^{-1} M_\odot$, which are most likely to retain a significant fraction of baryons in their dark matter potential wells. The chance of finding at least one of these massive secondary lenses intercepting a strong-lensing sight line (i.e. projected within a typical Einstein radius of $1''$ around the line centre, out to a redshift of 2) is about 10%. Depending on their density profiles, compact haloes (e.g. singular isothermal spheres) could generate severe astrometry anomalies with a probability of a few percent, while haloes with shallower inner profiles could not.

Fig. 10 presents the peculiar image configurations for an example sight line. Four, six and eight images (excluding the central image) are produced when the source is located at different positions with respect to two sets of tangential caustics. In this particular case, the second caustic is produced by a perturbing halo of $2 \times 10^{10} M_\odot$, modelled as a truncated singular isothermal sphere, projected near the centre of the main lens. Such peculiar image astrometry has already been proposed and used to constrain density profiles of massive intergalactic objects (e.g., Wyithe et al. 2001; Wilkinson et al. 2001).

5.2 Substructures inside line-of-sight haloes

To investigate the effect of substructures inside haloes along the line of sight, we have excluded all substructures from our Millennium-II lensing cones and calculated violations due to "smooth" line-of-sight haloes alone. Table 2 lists violation probabilities in this case (for different halo density profiles). The relevance of subhaloes to lensing flux-ratio anomalies strongly depends on their assumed density profiles. Above $m > 10^8 h^{-1} M_\odot$, NFW-like substructures within line-of-sight haloes are responsible for causing a few percent of the cusp-caustic violations.

5.3 Background vs. foreground

We have separated line-of-sight haloes that are distributed in front of and behind the main-lens plane ($z_d = 0.6$). The violation probabilities of these two groups are listed in Table 2, calculated excluding their subhaloes. A higher violation probability is found caused by haloes in the background than in the foreground, as more haloes intercept the light rays behind the main lens plane, given a typical lensing geometry ($z_d = 0.6$ and $z_s = 2$). It is interesting to notice that violations from the foreground and the background roughly add up to the total violations due to haloes along the entire line of sight (second row of Table 2). The ratio between violations from the foreground and from the entire sight line is close to 2:5, which is the ratio between the comoving radial distances for $z_d = 0.6$ and $z_s = 2$.

Table 3. Mean surface number densities of projected haloes out to $z = 2.0$ per decade of mass, averaged over 200 Monte-Carlo lensing cones.

$[10^6, 10^7]$	$[10^7, 10^8]$	$[10^8, 10^9]$	$[10^9, 10^{10}]$	$\geqslant 10^{10}$ ($h^{-1} M_\odot$)
414	50	6	0.7	0.1 (/arcsec^2)

6 RESULTS FROM MONTE-CARLO HALOES WITH A SHETH-TORMEN MASS FUNCTION

The Millennium-II simulation has a limited mass resolution. To investigate the mass dependence of the violation pattern below the halo mass of $10^8 h^{-1} M_\odot$, we have used a Monte-Carlo method to generate intergalactic halo populations with masses $10^6 h^{-1} M_\odot \leqslant m < 10^{12} h^{-1} M_\odot$ (see §7 for discussion on adopting $10^6 h^{-1} M_\odot$ as the lower mass limit). These haloes are drawn from the Sheth-Tormen mass function (Sheth & Tormen 2002) generated with the code provided by Reed et al. (2007).

We have randomly generated 200 lensing cones out to $z_s = 2$, each of which contains a main lensing halo modelled as an isothermal ellipsoid at redshift $z_d = 0.6$. The lensing strength $b_{\rm SIE}$ is fixed to be $0.84''$, the same as the mean $b_{\rm SIE}$ of the main lenses in the selected sample of the Millennium-II lensing cones. The axis ratio $q_3 = 0.8$, core radius $S_0 = 0.05''$ and an orientation angle of 0.25π are also taken to be the same for all main lenses.

In each realization of the lensing cone, line-of-sight halo positions are randomly generated, with number densities as given by the Sheth-Tormen mass function at the redshifts of the 60 lens planes used for the Millennium-II lensing cones. Table 3 lists the mean surface number densities of projected haloes in different mass decades, averaged over 200 lensing cones[4]. Haloes projected within the $50'' \times 50''$-cone are saved, and those projected within the central $5'' \times 5''$-region are modelled with truncated singular isothermal spheres and truncated NFW profiles (using both M08 and B01-M05 concentration-mass relations). Those further out are modelled with point masses. Cusp-caustic violations were identified in the same way as for the Millennium-II lensing cones.

[4] These numbers roughly follow a power-law mass function of $dn(m) = m^{-1.9} dm$, m being the mass of haloes.

Table 2. $P^{90}(R_{\rm cusp}^{0.187})$ from cosmological simulations.

Cases	truncated singular isothermal sphere	truncated NFW (M08)	truncated NFW (B01-M05)
haloes + subhaloes	7.8%	7.3%	12.8%
haloes only	7.0%	5.2%	9.7%
background haloes	5.0%	3.2%	5.8%
foreground haloes	2.0%	1.9%	4.0%

Note: $P^{90}(R_{\rm cusp}^{0.187}) \approx 10\%$ was derived using only substructure populations ($m \gtrsim 10^5 h^{-1} M_\odot$) from the Aquarius simulations (Xu et al. 2009, 2010). Cases here are using line-of-sight structures (haloes and subhaloes) from the Millennium II simulation ($m > 10^8 h^{-1} M_\odot$); subhaloes from the main lensing halo have been excluded.

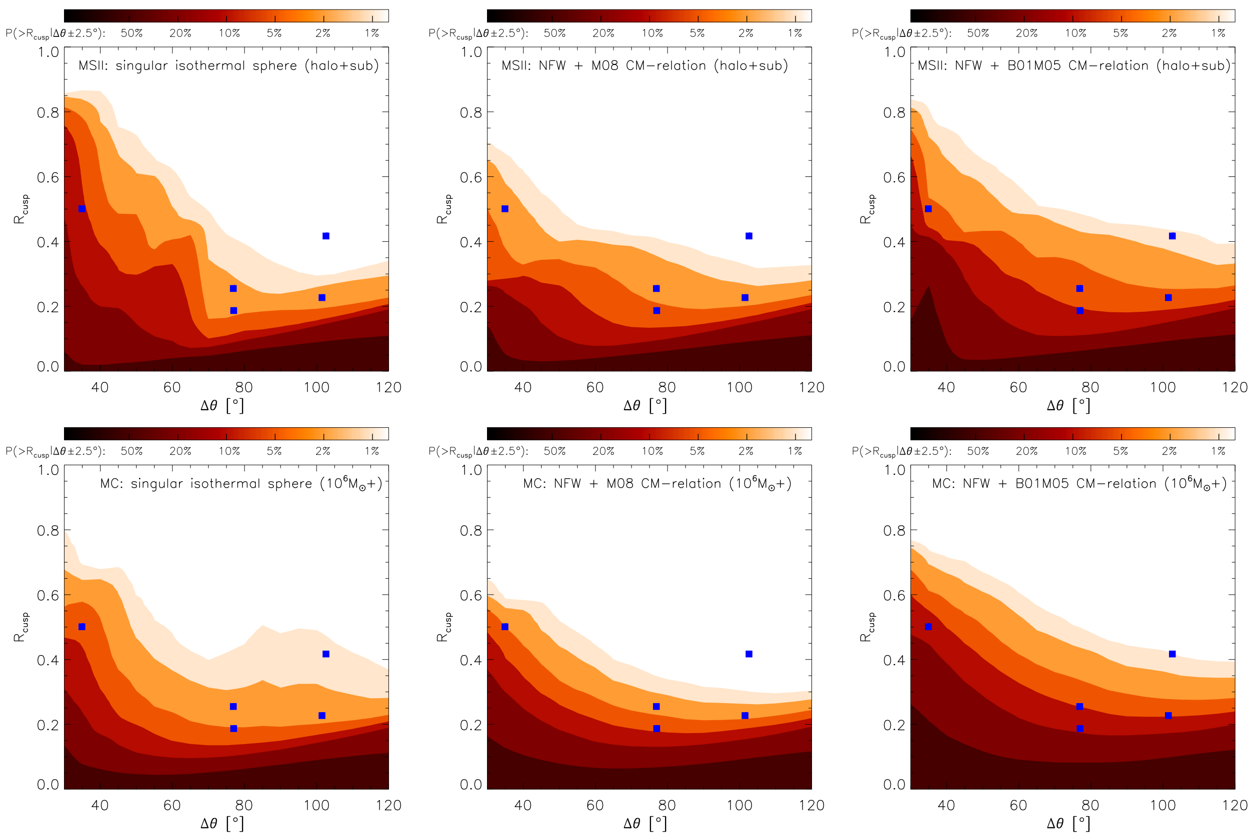

Figure 9. Contour maps of the violation probability $P(\geqslant R_{\rm cusp}|\Delta\theta \pm 2.5°)$. Symbols and contour levels are the same as in Fig. 3. The upper panels are for MS-II lensing cones with all line-of-sight haloes and subhaloes ($m > 10^8 h^{-1} M_\odot$), and the bottom panels are for Monte-Carlo lensing cones with line-of-sight haloes that follow the Sheth-Tormen mass function ($m \geqslant 10^6 h^{-1} M_\odot$). Three columns from left to right correspond to different assumptions for the density profile: truncated singular isothermal spheres, truncated NFW profiles with M08 and B01-M05 concentration-mass relations, respectively.

Table 4. Violation probabilities for Monte-Carlo lensing cones with main lens parameter $b_{\rm SIE} = 0.84''$.

$P^{90}(R_{\rm cusp}^{0.187})$	$\geqslant 10^6 h^{-1} M_\odot$	$\geqslant 10^7 h^{-1} M_\odot$	$\geqslant 10^8 h^{-1} M_\odot$	$\geqslant 10^9 h^{-1} M_\odot$	$\geqslant 10^{10} h^{-1} M_\odot$
truncated singular isothermal sphere	8.2%	7.7%	6.5%	4.8%	2.8%
truncated NFW profile (M08)	12%	9.1%	5.6%	2.5%	$< 1\%$
truncated NFW profile (B01-M05)	23%	18%	11%	5.5%	1.9%

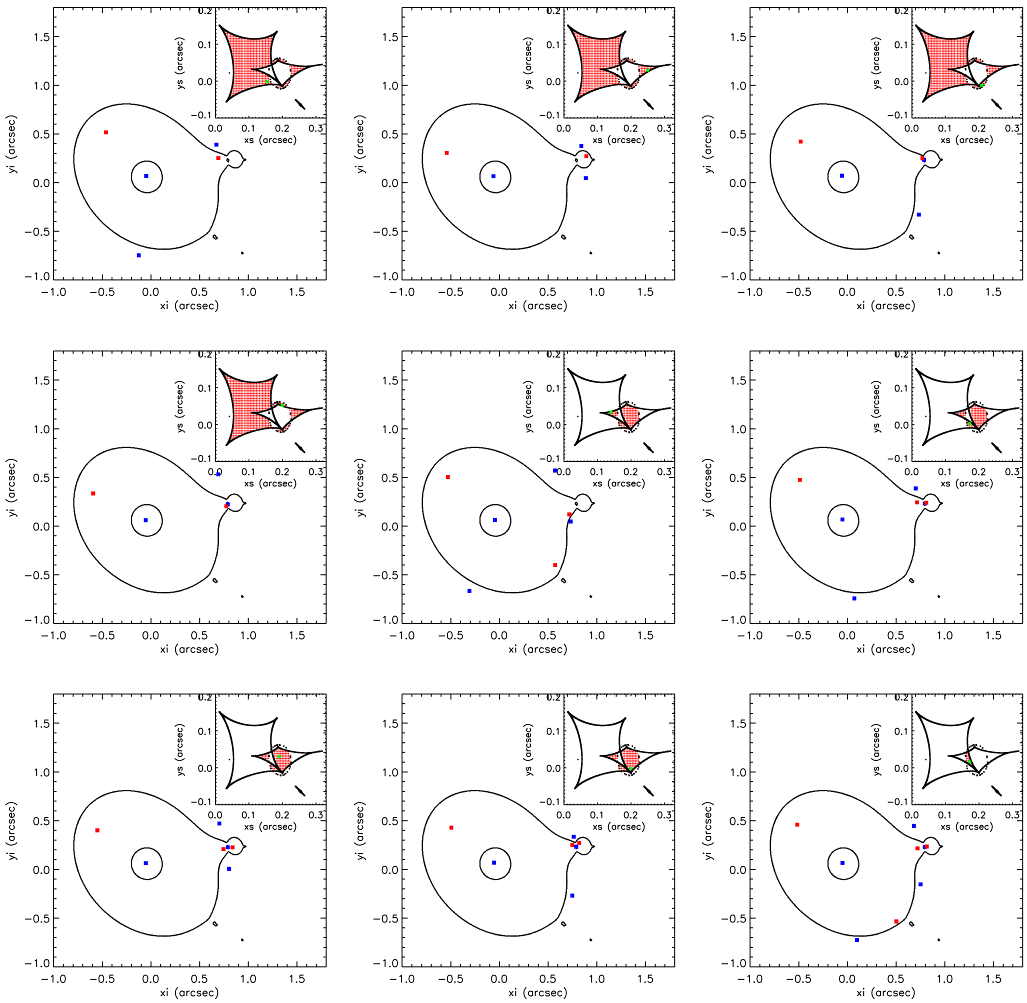

Figure 10. Critical curves and caustics of an example MS-II lensing cone. The remarkable wiggle feature on the tangential critical curve is caused by a $2 \times 10^{10} M_{\odot}$ halo along the line of sight, modelled as a truncated singular isothermal sphere. Green dots in red regions in the subpanels are example source positions. Red and blue dots in the main panels are the corresponding image positions; red for negative parities, blue for positive parities. Panels 1-4 present different image configurations for a source located within the caustic region where five images would be produced; panel 5-8 are for a caustic source with seven images; and panel 9 is for nine images.

6.1 Mass dependence of the cusp-caustic violation

The lower panels of Fig. 9 show $P(\geqslant R_{\rm cusp}|\Delta\theta \pm 2.5^{\circ})$ contour maps using Monte-Carlo realizations of the line-of-sight halo population, with a lower mass limit of $10^6 h^{-1} M_{\odot}$. As in the MS-II lensing case, the frequency of cusp-caustic violations depends strongly on the assumed halo density profiles. Table 4 also presents the values of $P^{90}(R_{\rm cusp}^{0.187})$ when this lower mass limit is increased, so that the mass dependence of the cusp-caustic violations can be seen.

Applying truncated singular isothermal spheres yields relatively larger contributions to cusp violations from more massive haloes[5] ($m \geqslant 10^{9\sim10} h^{-1} M_{\odot}$). When truncated NFW profiles are assumed, lower mass haloes would also cause a significant amount of violations. As can be seen from Table 4, when the lower mass limit of line-of-sight haloes decreases from $10^8 h^{-1} M_{\odot}$ to $10^6 h^{-1} M_{\odot}$ ($10^7 h^{-1} M_{\odot}$), the corresponding violation probabilities, $P^{90}(R_{\rm cusp}^{0.187})$, increase by $\sim$2% (1%), $\sim$6% (4%) and 12% (7%) when assuming truncated singular isothermal spheres and truncated NFW profiles with the M08 and the B01-M05 concentration-mass relations, respectively.

Comparing Table 4 with Table 2, it can be seen that our Monte-Carlo results are similar to those obtained using the Millennium-II lensing cones in the mass range above $10^8 h^{-1} M_{\odot}$. This suggests that the clustering of haloes is not a dominant effect in the production of flux-ratio anomalies for galactic-scale lenses.

[5] Xu et al. (2009) estimated the total lensing cross-section $\sigma_{\rm cs} \propto b_{\rm SIE}^2 \times N_{\rm perturbers}(m)$ for singular isothermal lenses. In this case $\sigma_{\rm cs} \propto m^{\alpha}$, and α is a positive value, hence the total lensing cross-section will be biased towards massive haloes.

6.2 Dependence on the Einstein radius

When the lower mass cutoff for main lensing haloes in the Millennium-II lensing cones is reduced from $10^{12} h^{-1} M_{\odot}$ to $10^{11} h^{-1} M_{\odot}$, the mean lensing strength $b_{\rm SIE}$ of the equiva-

Table 5. $P^{90}(R^{0.187}_{\rm cusp})$ for Monte-Carlo lensing cones with main lenses of different Einstein radii $b_{\rm SIE}$: violations due to line-of-sight perturbers more massive than $10^6 h^{-1} M_{\odot}$.

$P^{90}(R^{0.187}_{\rm cusp})$	$b_{\rm SIE} = 0.62''$	$b_{\rm SIE} = 0.84''$	$b_{\rm SIE} = 1.0''$	$b_{\rm SIE} = 1.5''$
truncated singular isothermal sphere	6.4%	8.2%	11%	15%
truncated NFW profile (M08)	9.5%	12%	15%	20%
truncated NFW profile (B01-M05)	20%	23%	28%	32%

lent isothermal ellipsoids decreases from $0.84''$ to $0.62''$ (corresponding to $\sigma_{\rm SIE} = 190\,{\rm km\,s^{-1}}$ for $z_d = 0.6$ and $z_s = 2$ using Eq.6). Table 5 presents the $P^{90}(R^{0.187}_{\rm cusp})$ values that result from four different $b_{\rm SIE}$ for the main lenses in our Monte-Carlo lensing cones. In addition to $b_{\rm SIE} = 0.62''$ and $0.84''$, we have calculated violations for an arbitrary $b_{\rm SIE}$ of $1''$ ($1.5''$), which is about the mean (largest) Einstein radius of the observed systems listed in Table 1.

As can be seen clearly from Table 5, systems with larger Einstein radii have higher violation probabilities. This is expected, because close triple images normally form around the tangential critical curve at about the Einstein radius. Comparing to the case of a small Einstein radius, a larger value of this radius results in a higher chance for the image triple (of a given opening angle $\Delta\theta$) to be intercepted by line-of-sight perturbers.

6.3 Halo concentrations and mass function

As we have shown above, the cusp-violation probability depends strongly on our assumptions about halo concentration. The concentration-mass relation derived by Bullock et al. (2001) has a simple functional form (including redshift evolution) and has been widely used in the literature. Colín et al. (2004) investigated concentration parameters for haloes of $10^6 h^{-1} M_{\odot} \leqslant m \leqslant 10^9 h^{-1} M_{\odot}$ and found this relationship to be a good fit. However, these early simulations of dark matter halo formation had relatively low numerical resolution and this can introduce systematic errors.

More recently, a number of authors including Neto et al. (2007), Gao et al. (2008), Zhao et al. (2009) and M08 (whose results are used above), derived concentration-mass relations from high-resolution cosmological N-body simulations. These studies are restricted to haloes with $m \geqslant 10^{10} h^{-1} M_{\odot}$ but they exhibit systematic differences from the concentrations obtained by B01-M05. For this reason we show lensing results using the M08 relation, extrapolating to lower masses when required, but exploring how the results change when this relation is varied by factors of a few.

The B01-M05 concentration-mass relation overestimates the concentration of small mass haloes inferred from the extrapolated M08 relation by factors of $3 \sim 4$ at $z = 0$. Therefore, we expect the violation probability to be larger for the B01-M05 relation than for the M08 relation. The scatter in halo concentration also affects the final cusp-violation probability.

Fig. 11 presents the values of $P^{90}(R^{0.187}_{\rm cusp})$ induced by line-of-sight haloes assuming the Sheth-Tormen mass function. To allow for possible uncertainties in halo concentration, we also show results for the case when the concentrations inferred from the M08 concentration-mass relation are multiplied by factors of 0.5, 1.0. 2.0 and 3.0. Varying amounts of scatter in concentration (for haloes of a given mass) are modelled assuming a Gaussian distribution with mean value equal to the M08 concentrations. As may be seen, the violation probabilities depend strongly on halo concentrations. Higher concentrations result in higher cusp-caustic violation probabilities. A larger scatter in concentration will also increase the violation probability.

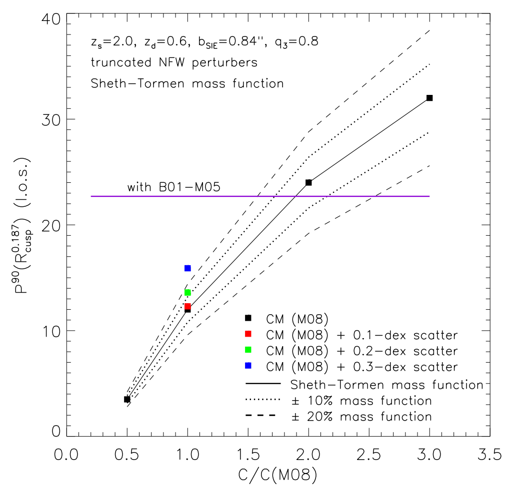

Figure 11. The violation probability $P^{90}(R^{0.187}_{\rm cusp})$ changes with the application of different concentration-mass relations. $P^{90}(R^{0.187}_{\rm cusp})$ is given by the Y-axis. The X-axis indicates the assumed halo concentration C (at any given mass) normalized to C(M08) – the concentration predicted by the M08 concentration-mass relation. The Sheth-Tormen mass function is used to generate line-of-sight halo populations. Values of $P^{90}(R^{0.187}_{\rm cusp})$ at C/C(M08)=0.5, 1.0, 2.0 and 3.0 are plotted as the four black squares, which are connected by the black solid line. Assuming that violations grow linearly with the number of perturbers, the dash and dotted lines plotting $(100 \pm 20)\%\times$ and $(100 \pm 10)\%\times$ the $P^{90}(R^{0.187}_{\rm cusp})$ values as shown in the black solid line, resemble violation probabilities under $(100\pm20)\%\times$ and $(100\pm10)\%\times$ the Sheth-Tormen mass function, respectively. Red, green and blue squares present results (under the Sheth-Tormen mass function) when allowing for scatter of concentrations (for haloes of a given mass) in form of Gaussian distributions with the standard deviation being 0.1, 0.2 and 0.3 dex around mean concentration values predicted by the M08 concentration-mass relation. $P^{90}(R^{0.187}_{\rm cusp})$ derived from using the B01-M05 concentration-mass relation is also given, indicated by the purple horizontal line.

The halo mass function (the number density of haloes per unit volume per decade in mass) influences the cusp violation probability. Metcalf (2005b) found that flux-ratio anomalies caused by line-of-sight perturbers not only depend strongly on the radial density profile of the haloes (their concentration), but also on the primordial matter power spectrum on small scales. Miranda & Macciò (2007) suggested that flux-ratio anomalies could be used statistically as a test of the behaviour of the matter power spectrum on small scales. We do not explore these effects here but in Fig. 11 we show the result of using $(100 \pm 10/20)\%\times$ the Sheth-Tormen mass function, and assuming that violations grow linearly with the number of perturbers.

7 DISCUSSION AND CONCLUSIONS

We have examined the effects of intergalactic cold dark matter haloes on flux-ratio anomalies in multiply-lensed quasar images by ray-tracing along strong-lensing sight lines that are either taken from the Millennium II simulation (for haloes and subhaloes with $m > 10^8 h^{-1} M_\odot$), or generated using the Monte-Carlo method assuming a Sheth-Tormen mass function (for haloes with $m \geqslant 10^6 h^{-1} M_\odot$).

We use $P^{90}(R_{\rm cusp}^{0.187})$, the probability for the cusp-caustic relation, $R_{\rm cusp}$, to be larger than or equal to 0.187 – the smallest value of $R_{\rm cusp}$ measured for cusp-caustic systems to date (for the quasar B1422) – over all realizations with $\Delta\theta \leqslant 90^\circ$, as a statistical measure of the cusp-caustic violation probability. We have found that the mean violation probability from intervening haloes depends strongly on their density profiles.

Chen et al. (2003) assumed singular isothermal spheres for line-of-sight haloes and find that they only contribute to $\leqslant$ 10% of the total perturbation. Assuming the same halo density profile, we find that the cusp-caustic violation probability caused by line-of-sight haloes with $m \geqslant 10^6 h^{-1} M_\odot$ is comparable to that caused by intrinsic substructures within the main lensing halo ($P^{90}(R_{\rm cusp}^{0.187}) \approx 8\%$ vs. 10%, Xu et al. 2010), which is in fair agreement with Miranda & Macciò (2007). The different results between Chen et al. (2003) and ours can be attributed to the drawbacks of their cross-section method, which underestimates effects from more sophisticated perturbation scenarios (see Metcalf 2005a).

When we assume truncated NFW profiles for the line-of-sight haloes ($m \geqslant 10^6 h^{-1} M_\odot$), the violation probability, $P^{90}(R_{\rm cusp}^{0.187})$, increases to 23% if we adopt the B01-M05 concentration-mass relation and to 12% if we adopt our preferred relation, that by M08. These values are larger than that due to the intrinsic subhalo populations alone.

A typical NFW profile has an Einstein radius $3 \sim 4$ orders of magnitude smaller than a singular isothermal sphere with a same mass. However, NFW perturbers in the mass range from $10^6 h^{-1} M_\odot$ to $10^{9\sim10} h^{-1} M_\odot$ cause more cusp violations than their singular isothermal counterparts. This may be due to the fact that in this mass range, perturbation in magnification (ratios) is mainly from fluctuations in the local density field that do not change the image positions. When comparing an NFW with a singular isothermal sphere of the same mass, we notice that the surface density distribution of the former exceeds that of the latter from a radius of $\sim 0.001 r_{200}$ outwards, which means the NFW profile is more effective in introducing fluctuation to the convergence and thus causing flux-ratio anomalies.

On the other hand, the deflection angle of a perturber of $m \sim 10^{6-9} h^{-1} M_\odot$ is always small ($\lesssim 0.001''$ for a singular isothermal sphere locating at $z = 0.6$), until the perturber is massive ($m \gtrsim 10^{10} h^{-1} M_\odot$) and compact enough (a singular isothermal sphere) to have a deflection angle ($\gtrsim 0.01''$) that can shift a nearby image to a new position with a different magnification from the primary lens (see Metcalf 2005b). This can explain the larger violation probabilities (as shown in Table 4), caused by singular isothermal perturbers of $m \geqslant 10^{9\sim10} h^{-1} M_\odot$ than by their NFW counterparts which are less effective in causing flux-anomalies due to shifting image positions.

Another issue concerns the finite-source effect. Metcalf & Amara (2010) pointed out that biased results about substructures could be drawn due to the point source approximation, which is used in this work.

The radio-emission regions of observed quasars are estimated to be ∼10 parsecs in extent (Andreani et al. 1999; Wyithe et al. 2002), corresponding to $\sim 0.001''$ for a source at $z_s = 2.0$. When the perturbing mass drops down below $10^6 h^{-1} M_\odot$, the corresponding effective perturbing area decreases to $\lesssim 0.001''$ in radius for the perturber at $z_d = 0.6$, becoming smaller than an image with $\mu \sim 10 - 20$ (around the tangential curve) of the radio emission region of a background quasar. As a result, the induced magnification fluctuation would be smeared out (within the image area), and thus no significant image flux anomaly would be observed at radio wavelengths (but could still be seen in the optical/near-infrared, which comes from much smaller physical regions. See Moustakas & Metcalf 2003 for spectroscopic gravitational lensing). This is why we do not consider the violation probability produced by perturbing haloes below $10^6 h^{-1} M_\odot$. As can be seen from Table 4, even if we neglect contributions from perturbers below $10^7 h^{-1} M_\odot$, we still find $\sim$ 10% cusp-violation probability from line-of-sight NFW-like perturbers adopting the M08 concentration-mass relation.

Several other points are worth noting. Firstly, the violation probability depends, of course, on the concentration of the halo, and both large halo concentrations and a large scatter in concentration will result in higher violation probabilities. Thus, it may be possible to use the statistics of flux-ratio distributions (measured in the radio) from large samples of lensed quasars to constrain the density profiles of low-mass dark matter haloes.

Secondly, systems with large Einstein radii are more likely to be observed in a configuration that violates the cusp-caustic relation because of a higher incidence of close triple images (with a given opening angle $\Delta\theta$) that are intercepted by line-of-sight perturbers. In our work, using the B01-M05 concentration-mass relation and adopting $b_{\rm SIE} = 1.0''$, the violation probabilities for several representative cases in Metcalf (2005a) can be reproduced.

Thirdly, the probability that a massive halo ($m \geqslant 10^{10} h^{-1} M_\odot$) intercepts a galaxy-scale strong-lensing sight line with an impact parameter of $\leqslant 1''$ from the main lens centre is about 10%. These halos can perturb image fluxes, surface brightness (e.g., Vegetti et al. 2009) and even image astrometry (e.g., Wyithe et al. 2001). Halos with compact density profiles (e.g., singular isothermal spheres) could generate extra image pairs locally with an image separation of

$0.01'' \sim 0.1''$, resulting in more than four bright images of a background quasar. With upcoming lensing surveys, observations of peculiar image configurations could put better constraints on the density profiles of these massive haloes (Orban de Xivry & Marshall 2009).

Fourthly, for masses above $10^8 h^{-1} M_\odot$, we find that halo clustering has only a minor effect on the flux-ratio anomalies for galaxy-scale lensing systems. For a typical lensing geometry (with $z_d = 0.6$, $z_s = 2$), the overall perturbation produced by background haloes (behind the main lens) is larger than that caused by foreground haloes.

To summarise, in this work we have calculated the cusp-caustic violation probability, as measured by $P^{90}(R^{0.187}_{\rm cusp})$, produced by line-of-sight dark matter haloes. The value of $P^{90}(R^{0.187}_{\rm cusp})$ strongly depends on halo density profiles, specifically on concentration, in the case of NFW perturbers. When the concentration-mass relation proposed by Macciò et al. (2008) is used, the value of $P^{90}(R^{0.187}_{\rm cusp})$ produced by all line-of-sight perturbers that could give rise to observable flux-ratio anomalies at radio wavelengths is found to be ∼10%. In previous work (Xu et al. 2009, 2010) using the Aquarius simulations (Springel et al. 2008), we had found that the contribution to $P^{90}(R^{0.187}_{\rm cusp})$ from intrinsic substructures within the main lensing galaxy and its dark matter halo amounts to $P^{90}(R^{0.187}_{\rm cusp}) \approx 10\%$. Summing up both contributions, the total violation probability could reach ∼20%.

There are five observed cusp geometry lensing systems whose triple images have opening angles $\Delta\theta \leqslant 90^\circ$. Of these, the three radio lensing cases show firm evidence for cusp-caustic violations due to galactic-scale structures. Applying the same statistical argument used by Xu et al. (2009), we conclude that the probability of observing such a violation rate (3/5) is ≈ 5% for a total $P^{90}(R^{0.187}_{\rm cusp}) \approx 20\%$. This can be compared with the probability of $< 1\%$ that Xu et al. (2010) found when considering only perturbations due to intrinsic substructures.

The existing observational sample is clearly too small for us to reach a definitive conclusion regarding the appropriateness of the ΛCDM model. Our main result, however, is that, depending on the density profiles of CDM haloes (and subhaloes), the line-of-sight projection effect on the flux-ratio anomalies of quasar images can be comparable to, or even larger than that from intrinsic subhalos. New multiply-lensed four-image systems discovered in upcoming lensing surveys will make it possible to use the statistics of flux-ratio anomalies to constrain the properties of dark matter halo as well as the cosmogonic model.

We mention in passing that a warm dark matter cosmogony has a different power spectrum of density perturbations, as well as different density profiles for small halos compared to the standard CDM cosmogony. This will result in different (presumably lower) cusp-violation probabilities (e.g., Miranda & Macciò 2007). This possibility is worth exploring further in future.

ACKNOWLEDGEMENTS

We thank Jie Wang, Houjun Mo, Leon Koopmans, Anna Nierenberg, Stefan Hilbert and Peter Schneider for helpful and insightful discussions. Thanks also go to Dr. Lydia Heck for her skillful management of and persistent dedication to the computer clusters at the Institute for Computational Cosmology in Durham, where the lensing simulations were carried out. SM acknowledges financial support from the Chinese Academy of Sciences, LG acknowledges support from an STFC advanced fellowship and a one-hundred-talents program of the Chinese Academy of Sciences (CAS) and the National Basic Research Program of China (973 program under grant No. 2009CB24901). CSF acknowledges a Royal Society Wolfson Research Merit award and an ERC advance investigator grant. REA acknowledges support from the Advanced Grant 246797 "GALFORMOD" from the European Research Council. This work was supported in part by an STFC rolling grant to the ICC.

REFERENCES

Amara A., Metcalf R. B., Cox T. J., Ostriker J. P., 2006, MNRAS, 367, 1367

Andreani P., Franceschini A., Granato G., 1999, MNRAS, 306, 161

Angulo R., 2008, PhD thesis, Institute for Computational Cosmology, University of Durham

Blandford R., Narayan R., 1986, ApJ, 310, 568

Boylan-Kolchin M., Springel V., White S. D. M., Jenkins A., Lemson G., 2009, MNRAS, 398, 1150

Bradač M., Schneider P., Lombardi M., Steinmetz M., Koopmans L. V. E., Navarro J. F., 2004, A&A, 423, 797

Browne I. W. A., Wilkinson P. N., Jackson N. J. F., Myers S. T., Fassnacht C. D., Koopmans L. V. E., Marlow D. R., Norbury M., Rusin D., Sykes C. M., Biggs A. D., Blandford R. D., de Bruyn A. G., Chae K. H., Helbig P., King L. J., McKean J. P., Pearson T., Phillips P., Readhead A., Xanthopoulos E., York T., 2003, MNRAS, 341, 13

Bullock J. S., Kolatt T. S., Sigad Y., Somerville R. S., Kravtsov A. V., Klypin A. A., Primack J. R., Dekel A., 2001, MNRAS, 321, 559

Chae K., Mao S., Kang X., 2006, MNRAS, 373, 1369

Chen J., Koushiappas S. M., Zentner A. R., 2011, ArXiv e-prints

Chen J., Kravtsov A. V., Keeton C. R., 2003, ApJ, 592, 24

Chiba M., 2002, ApJ, 565, 17

Colín P., Klypin A., Valenzuela O., Gottlöber S., 2004, ApJ, 612, 50

Dalal N., Kochanek C. S., 2002, ApJ, 572, 25

Davis M., Efstathiou G., Frenk C. S., White S. D. M., 1985, ApJ, 292, 371

Diemand J., Kuhlen M., Madau P., Zemp M., Moore B., Potter D., Stadel J., 2008, Nature, 454, 735

Fassnacht C. D., Blandford R. D., Cohen J. G., Matthews K., Pearson T. J., Readhead A. C. S., Womble D. S., Myers S. T., Browne I. W. A., Jackson N. J., Marlow D. R., Wilkinson P. N., Koopmans L., de Bruyn A., Schilizzi R., Bremer M., Miley G., 1999, AJ, 117, 658

Gao L., Navarro J. F., Cole S., Frenk C. S., White S. D. M., Springel V., Jenkins A., Neto A. F., 2008, MNRAS, 387, 536

Gao L., White S. D. M., Jenkins A., Stoehr F., Springel V., 2004, MNRAS, 355, 819

Helly J. C., Cole S., Frenk C. S., Baugh C. M., Benson A., Lacey C., 2003, MNRAS, 338, 903

Jackson N., Nair S., Browne I. W. A., Wilkinson P. N., Muxlow T. W. B., de Bruyn A. G., Koopmans L., Bremer M., Snellen I., Miley G. K., Schilizzi R. T., Myers S., Fassnacht C. D., Womble D. S., Readhead A. C. S., Blandford R. D., Pearson T. J., 1998, MNRAS, 296, 483
Katz C. A., Moore C. B., Hewitt J. N., 1997, ApJ, 475, 512
Keeton C. R., Gaudi B. S., Petters A. O., 2003, ApJ, 598, 138
Keeton C. R., Kochanek C. S., 1998, ApJ, 495, 157
Komatsu E., Dunkley J., Nolta M. R., Bennett C. L., Gold B., Hinshaw G., Jarosik N., Larson D., Limon M., Page L., Spergel D. N., Halpern M., Hill R. S., Kogut A., Meyer S. S., Tucker G. S., Weiland J. L., Wollack E., Wright E. L., 2009, ApJ Suppl., 180, 330
Komatsu E., Smith K. M., Dunkley J., Bennett C. L., Gold B., Hinshaw G., Jarosik N., Larson D., Nolta M. R., Page L., Spergel D. N., Halpern M., Hill R. S., Kogut A., Limon M., Meyer S. S., Odegard N., 2011, ApJ Suppl., 192, 18
Koopmans L. V. E., Biggs A., Blandford R. D., Browne I. W. A., Jackson N. J., Mao S., Wilkinson P. N., de Bruyn A. G., Wambsganss J., 2003, ApJ, 595, 712
Koopmans L. V. E., Treu T., Bolton A. S., Burles S., Moustakas L. A., 2006, ApJ, 649, 599
Macciò A. V., Dutton A. A., van den Bosch F. C., 2008, MNRAS, 391, 1940
Macciò A. V., Miranda M., 2006, MNRAS, 368, 599
MacLeod C. L., Kochanek C. S., Agol E., 2009, ApJ, 699, 1578
Mao S., Jing Y., Ostriker J. P., Weller J., 2004, ApJ Letters, 604, L5
Mao S., Schneider P., 1998, MNRAS, 295, 587
Marlow D. R., Myers S. T., Rusin D., Jackson N., Browne I. W. A., Wilkinson P. N., Muxlow T., Fassnacht C. D., Lubin L., Kundić T., Blandford R. D., Pearson T. J., Readhead A. C. S., Koopmans L., de Bruyn A. G., 1999, AJ, 118, 654
McKean J. P., Koopmans L. V. E., Flack C. E., Fassnacht C. D., Thompson D., Matthews K., Blandford R. D., Readhead A. C. S., Soifer B. T., 2007, MNRAS, 378, 109
Metcalf R. B., 2005a, ApJ, 622, 72
Metcalf R. B., 2005b, ApJ, 629, 673
Metcalf R. B., Amara A., 2010, ArXiv e-prints
Metcalf R. B., Madau P., 2001, ApJ, 563, 9
Metcalf R. B., Moustakas L. A., Bunker A. J., Parry I. R., 2004, ApJ, 607, 43
Metcalf R. B., Zhao H., 2002, ApJ Letters, 567, L5
Miranda M., Macciò A. V., 2007, MNRAS, 382, 1225
More A., McKean J. P., More S., Porcas R. W., Koopmans L. V. E., Garrett M. A., 2009, MNRAS, 394, 174
Moustakas L. A., Metcalf R. B., 2003, MNRAS, 339, 607
Myers S. T., Jackson N. J., Browne I. W. A., de Bruyn A. G., Pearson T. J., Readhead A. C. S., Wilkinson P. N., Biggs A. D., Blandford R. D., Fassnacht C. D., Koopmans L. V. E., Marlow D. R., McKean J. P., Norbury M. A., Phillips P. M., Rusin D., Shepherd M. C., Sykes C. M., 2003, MNRAS, 341, 1
Navarro J. F., Frenk C. S., White S. D. M., 1996, ApJ, 462, 563
Navarro J. F., Frenk C. S., White S. D. M., 1997, ApJ, 490, 493
Neto A. F., Gao L., Bett P., Cole S., Navarro J. F., Frenk C. S., White S. D. M., Springel V., Jenkins A., 2007, MNRAS, 381, 1450
Nierenberg A. M., Auger M. W., Treu T., Marshall P. J., Fassnacht C. D., 2011, ApJ, 731, 44
Oh S.-H., de Blok W. J. G., Brinks E., Walter F., Kennicutt Jr. R. C., 2011, AJ, 141, 193
Orban de Xivry G., Marshall P., 2009, MNRAS, 399, 2
Patnaik A. R., Kemball A. J., Porcas R. W., Garrett M. A., 1999, MNRAS, 307, L1
Puchwein E., Hilbert S., 2009, MNRAS, 398, 1298
Reed D. S., Bower R., Frenk C. S., Jenkins A., Theuns T., 2007, MNRAS, 374, 2
Rusin D., Kochanek C. S., 2005, ApJ, 623, 666
Rusin D., Kochanek C. S., Keeton C. R., 2003, ApJ, 595, 29
Schneider P., Ehlers J., Falco E. E., 1992, Gravitational Lenses. XIV, p. 560, Springer-Verlag Berlin Heidelberg New York
Schneider P., Weiss A., 1992, A&A, 260, 1
Sheth R. K., Tormen G., 2002, MNRAS, 329, 61
Spergel D. N., Verde L., Peiris H. V., Komatsu E., Nolta M. R., Bennett C. L., Halpern M., Hinshaw G., Jarosik N., Kogut A., Limon M., Meyer S. S., Page L., Tucker G. S., Weiland J. L., Wollack E., Wright E. L., 2003, ApJ Suppl., 148, 175
Springel V., 2005, MNRAS, 364, 1105
Springel V., Wang J., Vogelsberger M., Ludlow A., Jenkins A., Helmi A., Navarro J. F., Frenk C. S., White S. D. M., 2008, MNRAS, 391, 1685
Sugai H., Kawai A., Shimono A., Hattori T., Kosugi G., Kashikawa N., Inoue K., Chiba M., 2007, ApJ, 660, 1016
Treu T., Koopmans L. V. E., 2004, ApJ, 611, 739
Vegetti S., Koopmans L. V. E., 2009, MNRAS, p. 1456
Vegetti S., Koopmans L. V. E., Bolton A., Treu T., Gavazzi R., 2009, ArXiv e-prints 0910.0760
Wambsganss J., Bode P., Ostriker J. P., 2005, ApJ Letters, 635, L1
Wilkinson P. N., Henstock D. R., Browne I. W., Polatidis A. G., Augusto P., Readhead A. C., Pearson T. J., Xu W., Taylor G. B., Vermeulen R. C., 2001, Physical Review Letters, 86, 584
Wyithe J. S. B., Agol E., Fluke C. J., 2002, MNRAS, 331, 1041
Wyithe J. S. B., Turner E. L., Spergel D. N., 2001, ApJ, 555, 504
Xu D. D., Mao S., Cooper A. P., Wang J., Gao L., Frenk C. S., Springel V., 2010, MNRAS, 408, 1721
Xu D. D., Mao S., Wang J., Springel V., Gao L., White S. D. M., Frenk C. S., Jenkins A., Li G., Navarro J. F., 2009, MNRAS, 398, 1235
Zakharov A. F., 1995, A&A, 293, 1
Zhao D. H., Jing Y. P., Mo H. J., Börner G., 2009, ApJ, 707, 354